An Improved Electric Spring Topology Based on *LCL* Filter

Dongyuan Qiu, *Member, IEEE*, Changhai Yuan, Bo Zhang, *Senior Member, IEEE*, Mingbin Ke, Yanfeng Chen, *Member, IEEE*, and Fan Xie, *Member, IEEE*

***Abstract*—Electric spring (ES), which has been widely discussed in recent years, is a new demand response method. By adjusting the power of noncritical load (NCL), ES can adaptively improve power quality of the grid containing a high proportion of renewable energy sources. Most of the existing ESs is connected in series with NCLs, but this structure limits the compensation power range of ES. In this article, a new ES topology based on *LCL* filter is proposed, where NCL is paralleled with the capacitor branch as the shunt damper. Compared with other types of ES, the proposed *LCL*-ES has the advantages which can extend the adjustable power range, improve the voltage regulation performance, and suppress the inherent resonance spikes effectively. Finally, the feasibility of *LCL*-ES has been verified by simulation and experimental results.**

***Index Terms*—Demand response, electric spring (ES), *LCL* filter, microgrid, renewable energy source (RES).**

I. Introduction

With energy shortages, environmental pollution and climate changes becoming more and more serious, renewable energy source (RES) has received widespread attention. The power generation capacity of RES, such as wind and photovoltaics is increasing year by year. However, the inherent intermittence of RES makes it difficult to predict the power generation accurately. At the same time, the centralized control strategy has been widely used in the power system, where the power generation mainly depends on the prediction of power consumption. When a high proportion of RES is connected into the power grid, the mismatch between consumption and generation may occur, which will affect power quality, resulting in excessive voltage rises and supply-demand power imbalance [1]. Typical methods to solve the problem of power mismatch include tap-changing approach, reactive power compensation, and adoption of battery energy storage system (BESS) [2]. However, these existing approaches have some disadvantages such as real-time power imbalance, environmental concern, high cost of batteries.

Manuscript received May 14, 2021; revised August 14, 2021 and October 21, 2021; accepted November 27, 2021. Date of publication December 6, 2021; date of current version January 19, 2022. This work was supported by the Natural Science Foundation of Guangdong Province under Grants 2017B030312001 and 2020A1515011571. Recommended for publication by Associate Editor S. Golestan. *(Corresponding author: Dongyuan Qiu.)*

The authors are with the School of Electric Power Engineering, South China University of Technology, Guangzhou 510641, China (e-mail: epdyqiu@scut.edu.cn; 1115645087@qq.com; epbzhang@scut.edu.cn; 201921014973@mai.scut.edu.cn; eeyfchen@scut.edu.cn; epfxie@scut.edu.cn).

Color versions of one or more figures in this article are available at https://doi.org/10.1109/TPEL.2021.3132907.

Digital Object Identifier 10.1109/TPEL.2021.3132907

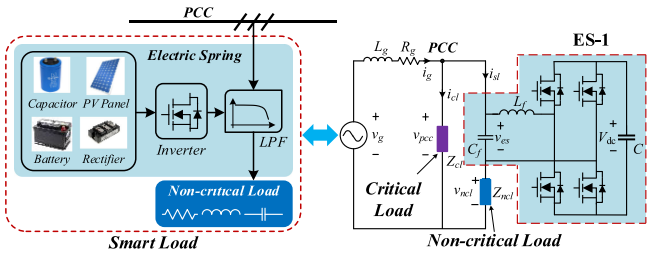

Fig. 1. General connection way among ES, NCL, and CL.

In recent years, a demand response based on electric spring (ES) has been proposed and used to enhance the voltage and frequency stability, power balance, and harmonic suppression in a distribution network [3]. Its core idea is to shift the voltage or power fluctuations from upstream of the point of common coupling (PCC) to noncritical load (NCL), in order to achieve the stabilization of voltage on PCC or critical load (CL).

The concept of ES was first proposed in 2012, where ES and NCL are connected in series to form a smart load (SL), then SL is connected in parallel with CL. Most of ESs appeared later use the similar connection way, as shown in Fig. 1 [4]. From the perspective of topology, ES can be divided into three main generations and other variants. ES-1 can only perform reactive power compensation due to no battery storage on the dc side [3]. ES-2 with battery storage can compensate both active and reactive power in eight different combination modes [5]–[7]. ES-3 is a special case because its topology is similar to the BESS [8]. Thus, most of ES variants are improved on the basis of ES-2, such as B2B-ES in which the dc-link voltage comes from an ac–dc converter [9], PV-ES in which the battery storage is replaced by the photovoltaic system [2], hybrid-ES combining the renewable generations with battery storages [10]. Different types of single ES all show the fast demand-side management performance under appropriate control strategies [11]–[14]. Compared with other demand response methods, ES has another advantage which can be distributed in the power grid to provide strong stability support [4]. Models of distributed ESs have been developed to demonstrate the effectiveness of installing a large number of ESs in the power grid [15]–[18]. Droop control without communication and consensus control with communication are widely used to realize the group operation of ESs [19]–[21], and a centralized predictive control

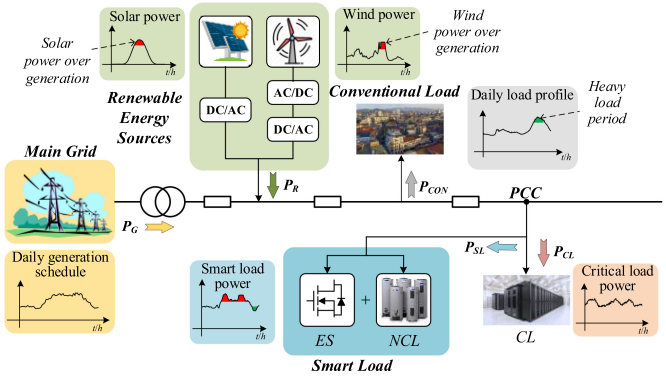

Fig. 2. Power flow in a microgrid.

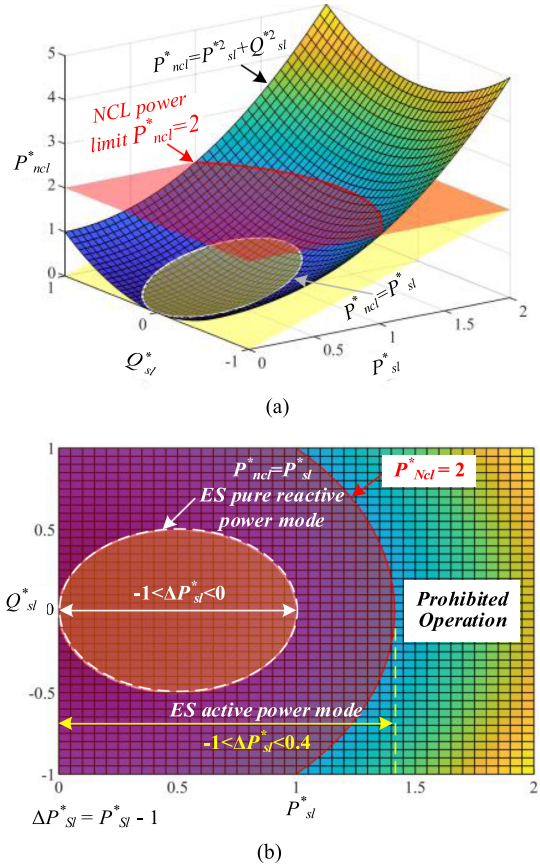

Fig. 3. Power range sketch of series-ES. (a) $P^*_{ncl}, P^*_{sl}, Q^*_{sl}$. (b) Power range of series-ES based SL (top view).

was proposed for distributed ESs to further reduce distribution power loss [22].

Although multiple ESs can provide the necessary voltage control for the CLs at different nodes in the distribution network, the contribution of a single ES is still limited by the capacity of the NCL connected to it. In order to solve the limitations brought by NCL, the connection between ES and NCL should be changed. *LCL* filters have been widely used in grid-connected inverters due to their excellent harmonic suppression, size and cost [23]. Among the various suppression methods for resonance spikes, resistor in parallel with filter capacitor can achieve the best balance of spike suppression and high-frequency suppression, but it will bring significant power loss in practice [24]. In this article, a passively damped *LCL*-ES is proposed by deploying NCL in parallel with the capacitor branch of *LCL* filter.

The rest of this article is organized as follows. Section II proves that the performance of SL is related to NCL. Then in Section III, topology of the proposed *LCL*-ES is presented together with its operating principle. A critical design process of *LCL*-ES is described in Section IV. Simulation and experimental results of *LCL*-ES are given in Sections V and VI, respectively. Finally, Section VII concludes this article.

II. Power Analysis of Series-ES

From the perspective of power flow, the reason for the voltage fluctuations at the PCC is that the power does not match in real time. The large-scale renewable energy injected into the grid will exacerbate this imbalance [25]. Due to the large resistance and inductance ratio of low-voltage distribution lines, the fluctuation of the active power flow dominates the voltage fluctuation in the distribution network. In order to achieve the best voltage regulation effect, it is hoped that the NCL can undertake the task of active power compensation, that is, the active power fluctuation should be transferred to the NCL as much as possible. Fig. 2 shows the schematic diagram of the inflow and outflow power at the PCC in a microgrid. When the renewable energy generation is too large, it will cause the PCC voltage to rise, and the ES will force the NCL power to increase in order to balance power and voltage, and vice versa. With the engagement of ES, the power mismatch is transferred to NCL.

In this article, the ES connected in series with NCL is called series-ES. The power relationship of series-ES is discussed below. In order to facilitate the analysis, it is assumed that $Z_{\rm ncl} = R_{\rm ncl}$. When the PCC voltage $V_{\rm pcc}$ is stable, the relationship among NCL power $P_{\rm ncl}$, SL active power $P_{\rm sl}$ and reactive power $Q_{\rm sl}$ is

$$P_{\rm ncl} = \frac{R_{\rm ncl}(P_{\rm sl}^2 + Q_{\rm sl}^2)}{V_{\rm pcc}^2}. \tag{1}$$

Assuming the power reference as $S_n = V_n^2/R_{ncl}$, where V_n is the nominal RMS of $v_{\rm pcc}$, the per-unit form of (1) can be derived as

$$P^*_{ncl} = {\rm P}^{*2}_{sl} + {\rm Q}^{*2}_{sl} \tag{2}$$

where $P^*_{ncl} = P_{ncl}/S_n$, $P^*_{sl} = P_{sl}/S_n$, and ${\rm Q}^*_{sl} = {\rm Q}_{sl}/S_n$.

Considering the power limit of NCL is 2 p.u., the power surface of the series-ES can be drawn according to (2), as shown in Fig. 3(a). The power range of SL can be visualized considering the interception points between the plane $P^*_{\rm ncl} = 2$ p.u. and the paraboloid function in (2) as indicated in Fig. 3(b). Then the compensation range $\Delta P^*_{\rm sl}$ of SL can be measured by the difference between $P^*_{\rm sl}$ and 1, that is $\Delta P^*_{\rm sl} = P^*_{\rm sl} - 1$.

According to Fig. 3, if series-ES operates in pure reactive power mode, then $P_{\rm ncl} = P_{\rm sl}$ and no dc source is needed. The

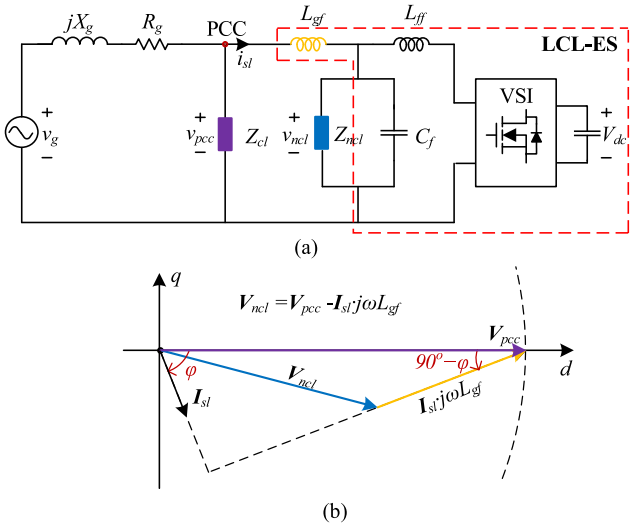

Fig. 4. Topology and phasor diagram of *LCL*-ES. (a) *LCL*-ES topology (Single phase). (b) Phasor diagram.

power range of SL is illustrated by the white dotted line in Fig. 3(b), it can be seen that the compensation range is $-1 < \Delta P^*_{\rm sl} < 0$ p.u., which means that only the negative active power compensation can be achieved.

III. Topology and Operating Principle of *LCL*-ES

A. Topology of LCL-ES

The proposed *LCL*-ES is shown in Fig. 4(a), the output of VSI is connected to an *LCL* filter, L_{ff} is filter inductor and L_{gf} is the grid-connected inductor, while NCL is paralleled with filter capacitor C_f. Thus, the voltage across C_f is equal to the voltage on NCL v_{ncl}. In the steady state, the PCC voltage phasor $\boldsymbol{V}_{\rm pcc}$ and NCL voltage phasor $\boldsymbol{V}_{\rm ncl}$ have the following relationship:

$$\mathbf{V}_{\rm ncl} = \mathbf{V}_{\rm pcc} - j\omega_o L_{gf}\mathbf{I}_{\rm sl} = \mathbf{V}_{\rm pcc} - jZ_g\mathbf{I}_{\rm sl} \tag{3}$$

where ω_o is the fundamental angle frequency.

According to the phasor diagram in Fig. 4(b), the amplitude of $\boldsymbol{V}_{\rm ncl}$ can be derived as

$$V_{\rm ncl} = \sqrt{(Z_g I_{\rm sl})^2 + V_{\rm pcc}^2 - 2V_{\rm pcc}Z_g I_{\rm sl}\sin\varphi}. \tag{4}$$

Similarly, when $V_{\rm pcc}$ is stable, $V_{\rm pcc} = V_n$, the following per-unit relationship can be derived

$$P^*_{\rm ncl} = 1 + a^2(P^{*2}_{\rm sl} + Q^{*2}_{\rm sl}) - 2aQ^*_{\rm sl} \tag{5}$$

where $a = Z_g/R_{\rm ncl}$.

The power surfaces of different a are drawn in Fig. 5. As a increases, the power range and its projection on the horizontal plane will decrease. Substituting $P^*{}_{\rm ncl} = P^*{}_{\rm sl}$ into (5), the power relationship between $P^*{}_{\rm ncl}$ and $Q^*{}_{\rm sl}$ in pure reactive mode is shown in Fig. 6. The limit of apparent power $S^*{}_{\rm SL\_lim} = 3$ is set by considering the total capacity limitation or output overcurrent protection of the SL. It can be found that $P^*{}_{\rm ncl}$ for *LCL*-ES can be greater than 1 while series-ES cannot, thus

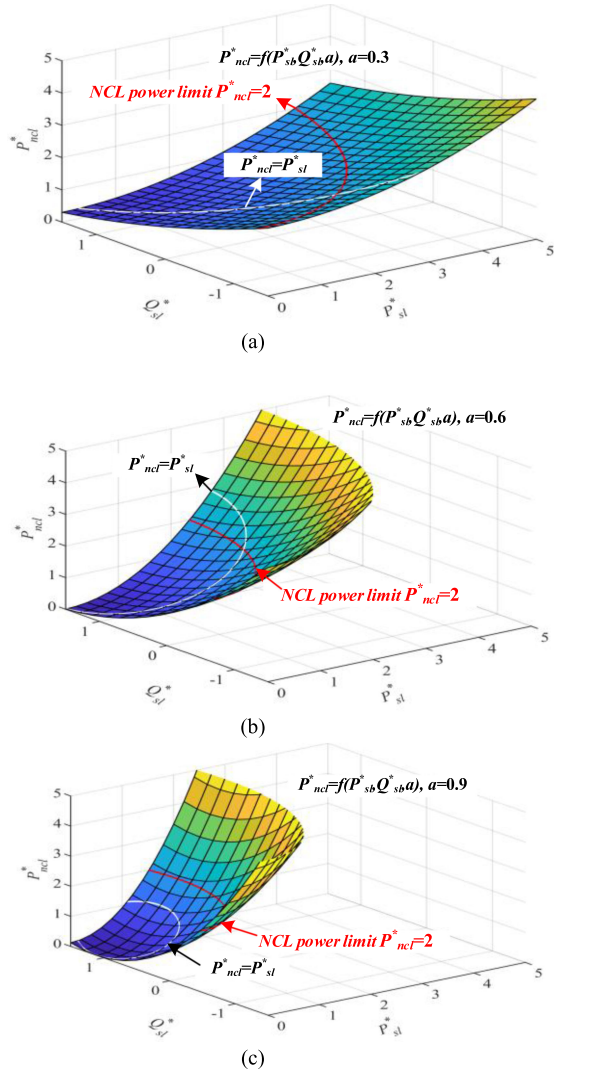

Fig. 5. *LCL*-ES power surfaces of different a. (a) $a = 0.3$. (b) $a = 0.6$. (c) $a = 0.9$.

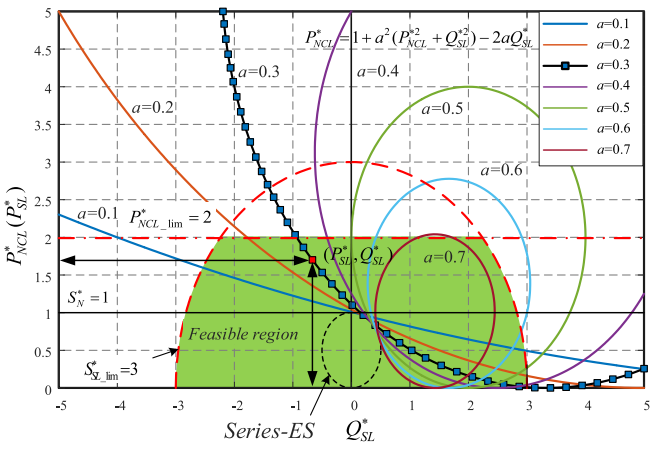

Fig. 6. *LCL*-ES compensation range under reactive power mode.

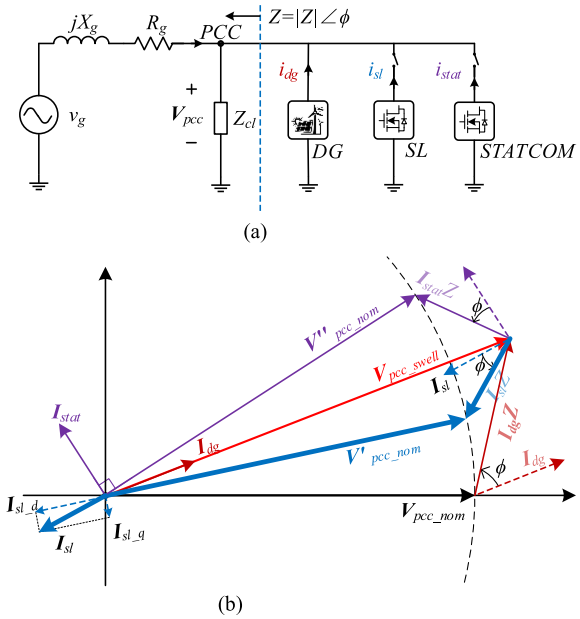

Fig. 7. Comparison between *LCL*-ES and STATCOM. (a) Simplified circuit of distributed system. (b) Phasor diagram comparison.

the *LCL*-ES has greater power range than series-ES. In order to obtain a sufficiently large compensation range within the limited range (the green area in Fig. 6), the value of a should be selected reasonably. When $a = 0.3$, $P^*_{\rm sl}$ ranges from 0 to 2 (corresponding to -1 to 1 for $\Delta P^*_{\rm sl}$).

B. Voltage Regulation Principle

Most of the existing ESs is based on voltage control strategies, but *LCL*-ES here adopts current control strategy, whose compensation principle is similar to that of DSTATCOM or SAPF with voltage regulation function [26].

As shown in Fig. 7(a), a distributed generator (DG) is installed at the end of distribution line, which may cause PCC voltage swell from $\boldsymbol{V}_{\rm pcc\_nom}$ to $\boldsymbol{V}_{\rm pcc\_swell}$. Both STATCOM and *LCL*-ES are equipped to keep the PCC voltage stable. In order to highlight the difference between STATCOM and *LCL*-ES, Fig. 7(b) shows the effect when they work alone. It is found that STATCOM only injects reactive power to stabilize the PCC voltage, which will enlarge power angle difference and may deteriorate the stability of power system [27]. However, *LCL*-ES can stabilize the PCC voltage and reduce the power angle difference by injecting active power and reactive power.

C. Model of LCL-ES

Fig. 8(a) shows the equivalent model of single-phase *LCL*-ES, in which $G_i(s)$ is the inner controller, H_i is the sampling coefficient. For simplicity, all ESRs of the passive components are neglected, which represents the worst case in terms of damping. The simplified model as shown in Fig. 8(b) can be obtained via transformation, where the transfer function $G_{x1}(s)$ and $G_{x2}(s)$ are defined by

$$\begin{cases} G_{x1}(s) = \frac{K_{\rm PWM}R_{\rm ncl}\cdot G_i(s)}{s^2L_{gf}C_fR_{\rm ncl}+sL_{gf}+R_{ncl}} \\ G_{x2}(s) = \frac{s^2R_{\rm ncl}L_{gf}C_f+sL_{gf}+R_{\rm ncl}}{s^3L_{gf}L_{ff}R_{\rm ncl}C_f+s^2L_{gf}L_{ff}+s(L_{gf}+L_{ff})R_{\rm ncl}}. \end{cases} \tag{6}$$

Then, the loop gain $T_A(s)$ can be expressed by

$$T_A(s) = G_{x1}(s)G_{x2}(s)H_i = \frac{H_iK_{\rm PWM}}{L_{ff}L_{gf}C_f} \cdot \frac{G_i(s)}{s(s^2+2\zeta\omega_r s+\omega_r^2)} \tag{7}$$

where $\omega_r = 2\pi f_r$ is the resonant frequency, ζ is the damping coefficient, and their corresponding representation are

$$\begin{cases} \omega_r = 2\pi f_r = \sqrt{\frac{L_{ff}+L_{gf}}{L_{ff}L_{gf}C_f}} \\ \zeta = \frac{1}{2\omega_rC_fR_{\rm ncl}} = \frac{a}{2\omega_rC_f\omega_oL_{gf}}. \end{cases} \tag{8}$$

Based on Fig. 8(b), the expression of $i_{\rm sl}$(s) is

$$\begin{aligned} i_{\rm sl}(s) &\triangleq \frac{1}{H_i}\frac{T_A(s)}{1+T_A(s)}i^*_{\rm sl}(s) - \frac{G_{x2}(s)}{1+T_A(s)}v_{\rm pcc}(s) \\ &= i_{\rm sl1}(s) + i_{\rm sl2}(s). \end{aligned} \tag{9}$$

It can be seen that $i_{\rm sl}(s)$ is composed of the instruction tracking component $i_{\rm sl1}$(s) and the disturbance component $i_{\rm sl2}(s)$ caused by PCC voltage. In order to eliminate the disturbance component $i_{\rm sl2}(s)$, PCC voltage feedforward is used. As shown in Fig. 8(b), branch $G_{x2}(s)$ can be added between $v_{\rm pcc}(s)$ and $i_{\rm sl}(s)$. Then, $G_{x2}(s)$ is removed and $1/G_{x1}(s)$ is inserted between $v_{\rm pcc}(s)$ and $i_{\rm sl\_ref}(s)$. In practice, the feedforward function $G_{x1}(s)$ can be equivalently transformed into three parts as shown in Fig. 8(c), which will be discussed later.

D. Damping Effect of NCL

According to (7) and (8), the frequency response of untuned $T_A(s)$ with $G_i(s) = 1$ is shown in Fig. 9. The resonant peak can be damped better with smaller $R_{\rm ncl}$, but the phase response will be quite sensitive, which may significantly impact the stability. Obviously, it is required that the control bandwidth cannot exceed or even be close to the resonance frequency, due to the insufficient phase margin for closed-loop control. When $R_{\rm ncl}$ is chosen to be 5Ω and the crossover frequency is set to be $f_c = 0.3f_r$, considering the nonnegligible delays caused by sampling and modulation, the phase margin of *LCL*-ES system will be 65°, which is acceptable as compared to 90° of *L* filter [28].

In order to ensure the tracking performance, f_c should be much higher than the fundamental frequency f_o or the highest harmonic of compensation f_h. The switching frequency f_s should be greater than $2f_r$ for the attenuation of switching harmonics. Generally speaking, the bandwidth of the system shall meet the following relationship:

$$f_o \ll f_c \le 0.3f_r < 2f_r \le f_s. \tag{10}$$

Actually, the *LCL*-ES mentioned here is an application of the passive damping method, where the resistive NCL paralleled with filter capacitor is treated as a shunt damper. Meanwhile, the shunt damper will not interfere with the high-frequency

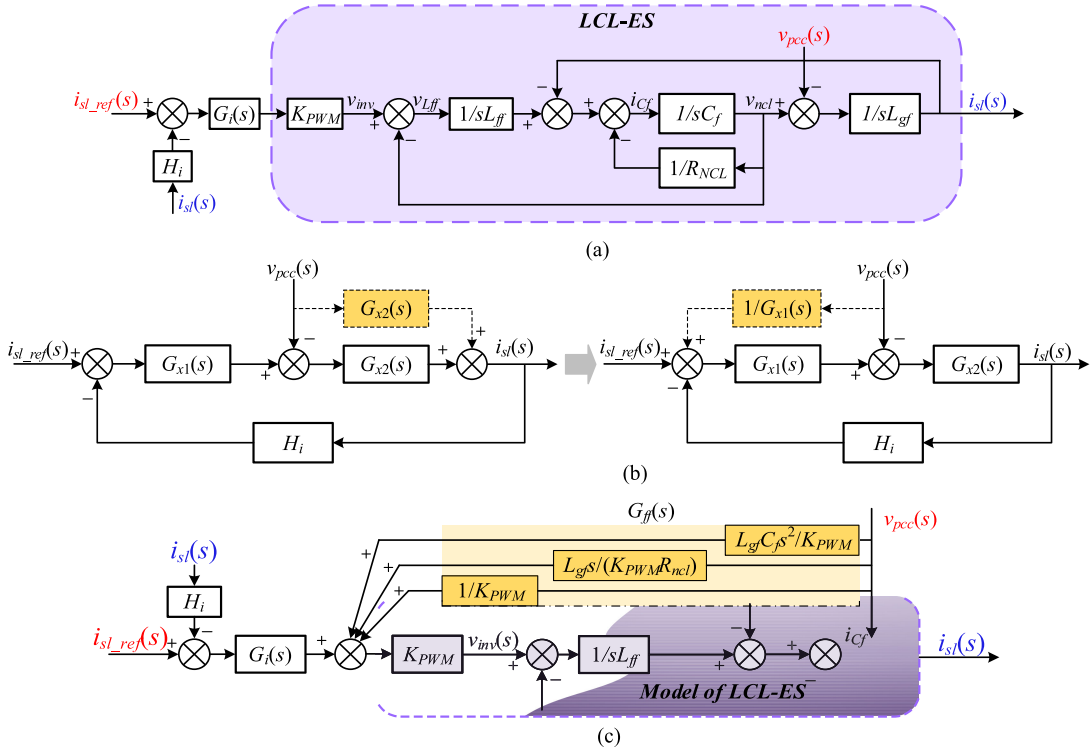

Fig. 8. Model and PCC voltage feedforward of *LCL*-ES. (a) Model of *LCL*-ES. (b) Simplified model with PCC feedforward. (c) PCC feedforward function $G_{ff}(s)$.

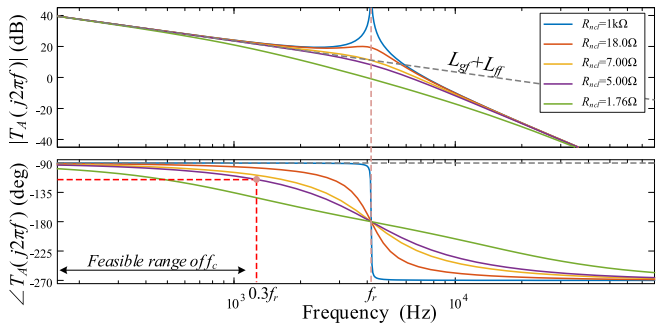

Fig. 9. Bode diagram of $T_A(s)$.

characteristics of the *LCL* filter, which is critical for superior switching harmonic suppression and much reduced volume of passive elements [29]. On the contrary, the other passive damping methods cannot achieve fast attenuation at high frequency.

IV. Control and Design of *LCL*-ES

A. Inner and Outer Control Loop

According to magnitude characteristic in Fig. 9, when frequency is lower than the cut-off frequency f_c, $T_A(s)$ of *LCL*-ES is similar to that of *L* filter, which means that *LCL*-ES can be treated as a grid-connected inverter with L_{gf}+L_{ff} filter [28]. The approximated $|T_A(s)|$ is obtained as follows:

$$|T_A(s)| \approx \left| \frac{H_i K_{\mathrm{PWM}} G_i(s)}{s(L_{gf}+L_{ff})} \right|. \tag{11}$$

When PI controller $G_i(s) = K_p + K_i/s$ is used in the inner current loop, the proportional coefficients K_p can be easily calculated as follows [30]:

$$K_p \approx \frac{2\pi f_c (L_{gf}+L_{ff})}{H_i K_{\mathrm{PWM}}}. \tag{12}$$

As for the integral coefficient K_i, the larger it is, the smaller the steady-state error is. So far, the related models and designs of *LCL*-ES are similar to those of grid-connected inverters. However, in the ES based demand response, it is necessary to control the NCL to participate in stabilizing of PCC voltage instead of adjusting the grid-connected power. Therefore, in order to adjust the PCC voltage within the stable range of the system, the other parameters including K_i need to be specially designed, which will be given later.

As shown in Fig. 10, the outer voltage control includes a PCC voltage loop and a dc voltage loop, which respectively determine the *q*-axis and *d*-axis current reference. The PCC voltage loop is designed to maintain the rms of v_{pcc} within the acceptable range, while the dc voltage loop is to keep V_{dc} constant, which is critical for *LCL*-ES operating in pure reactive power mode. It is worth noting that the PCC voltage loop can adjust reactive power and active power at the same time, according to Fig. 6. These two voltage loops are strongly coupled, which is different from the decoupling of active and reactive power in grid-connected inverters. Finally, the bandwidths of outer loops should be much slower than the inner current loop to avoid interference.

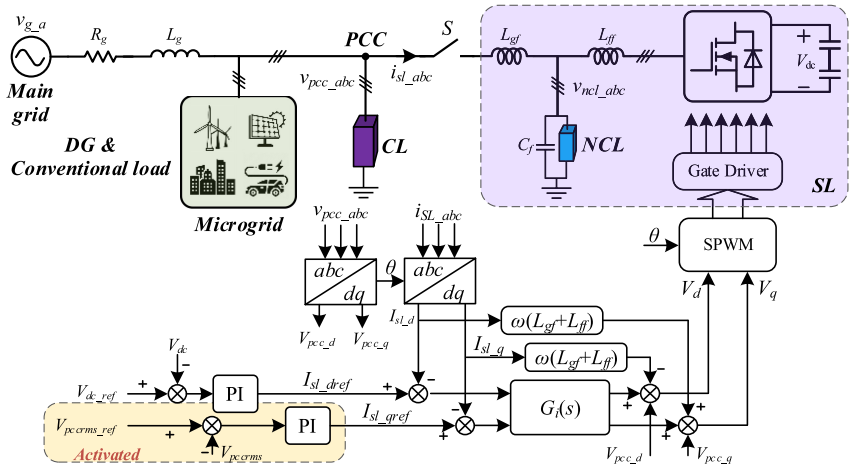

Fig. 10. General diagram of control loops.

B. PCC Voltage Feedforward

PCC voltage feedforward is an effective and simple method to eliminate the disturbance [31]. The feedforward signal is superimposed into the modulation wave directly, and the feedforward function $G_{ff}(s)$ is defined by

$$G_{ff}(s)=\frac{G_i(s)}{G_{x1}(s)}=\frac{1}{K_{\mathrm{PWM}}}\left(1+\frac{L_{gf}}{R_{\mathrm{ncl}}}s+L_{gf}C_f s^2\right). \tag{13}$$

It is found that $G_{ff}(s)$ is composed of a proportional term, a first differential term and a second differential term. Obviously, the commonly used proportional feedforward method cannot completely eliminate the disturbance.

C. Parameter Design

Based on the topology of *LCL*-ES, the terminal voltage of NCL can be regulated by adjusting the grid-connected current. Therefore, the filter design of *LCL*-ES is different from those commonly used for *LCL* filter. First of all, the power compensation range of *LCL*-ES must be guaranteed, and then the system control performance should meet the requirements. According to the aforementioned analysis, the active power range of *LCL*-ES as a demand response is closely related to the NCL or the actual load used as NCL and parameter a. Once NCL is determined, R_{ncl} can be determined. Adjusting a can significantly change the power characteristics, as shown in Fig. 6, thereby affect compensation range or power range of *LCL*-ES.

When R_{ncl} and a are known, L_{gf} can be determined, and then the remaining parameters can be determined. First, according to the highest compensation harmonics, switching frequency and fundamental frequency, (12) is used to determine f_r and f_c. Then, considering the control performance constraints from steady-state error and stability margin, the remaining parameters can be determined.

After adopting the PCC voltage feedforward strategy, the steady-state error E_r of the current inner loop is

$$E_r=\left|\frac{I_{\mathrm{sl\_ref}}-H_iI_{\mathrm{sl}}}{I_{\mathrm{sl\_ref}}}\right|\approx\frac{1}{|1+T_A(j2\pi f_o)|}\approx\frac{1}{|T_A(j2\pi f_o)|} \tag{14}$$

where $I_{\mathrm{sl\_ref}}$ and I_{sl} are the effective values of $i_{\mathrm{sl\_ref}}$ and i_{sl}, respectively. Under the requirement of E_r, replacing $G_i(s)$ with PI controller can get the loop gain amplitude T_{fo} at the fundamental frequency f_o as

$$T_{fo}=20\lg|T_A(j2\pi f_o)|=20\lg\left|\frac{H_iK_{\mathrm{PWM}}}{(2\pi f_o)^2}\frac{j2\pi f_oK_p+K_i}{L_{gf}+L_{ff}}\right|. \tag{15}$$

After substituting K_p given by (12), the constraint K_{i_Tfo} can be obtained as follows:

$$K_{i\_Tfo}=\frac{4\pi^2f_o(L_{gf}+L_{ff})}{H_iK_{\mathrm{PWM}}}\sqrt{10^{T_{fo}/10}f_0^2-f_c^2}. \tag{16}$$

In order to avoid the error caused by the approximation, substituting K_{i_Tfo} given by (16) into (7), the phase margin PM of the system can be calculated as

$$\mathrm{PM}=\arctan\frac{2\pi R_{ncl}C_f(f_r^2-f_c^2)}{f_c}-\arctan\frac{K_i}{2\pi f_cK_p}. \tag{17}$$

Furthermore, the constraint K_{i_PM} can be obtained as

$$K_{i\_\mathrm{PM}}=2\pi f_cK_p\frac{2\pi C_fR_{\mathrm{ncl}}(f_r^2-f_c^2)-f_c\tan\mathrm{PM}}{2\pi C_fR_{\mathrm{ncl}}(f_r^2-f_c^2)\tan\mathrm{PM}+f_c}. \tag{18}$$

Under the constraints of T_{fo} and PM, substitute $K_{i\_Tfo}=K_{i\_\mathrm{PM}}$ into (18), and then substitute (12) into (18) to get the constraints of parameter $R_{ncl}C_f$

$$R_{\mathrm{ncl}}C_{f\_Tfo\_\mathrm{PM}}=\frac{f_c(f_c^2\tan\mathrm{PM}+f_o\sqrt{10^{T_{fo}/10}f_0^2-f_c^2})}{2\pi(f_r^2-f_c^2)(f_c^2-f_o\tan\mathrm{PM}\sqrt{10^{T_{fo}/10}f_0^2-f_c^2})}. \tag{19}$$

Since the phase-frequency characteristic of T_A crosses -180^{o} at f_r, its amplitude margin GM is

$$\mathrm{GM}=-20\lg|T_A(j2\pi f_r)|. \tag{20}$$

The PI controller $G_i(s)$ can be regarded as K_p at high frequency, substituting (7) and (12) into (20) can solve the GM constraint on $R_{\mathrm{ncl}}C_f$ as

$$R_{\mathrm{ncl}}C_{f\_\mathrm{GM}}=\frac{10^{-\mathrm{GM}/20}}{2\pi f_c}. \tag{21}$$

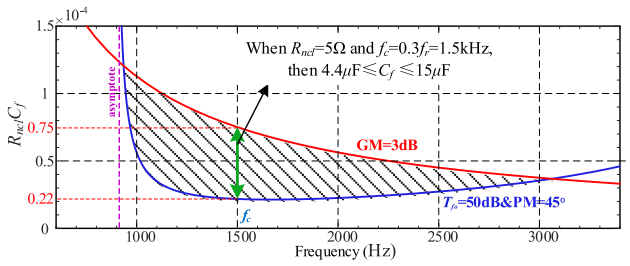

Fig. 11. Feasible region of $R_{\mathrm{ncl}}C_f$.

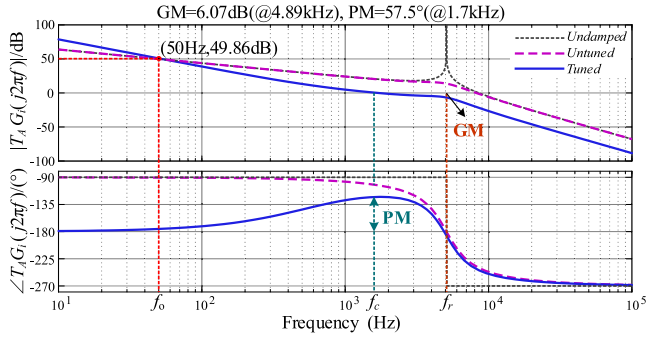

Fig. 12. Bode of loop gain before and after turning.

Based on the above analysis, the specific design steps are as follows.

Step 1: Determine the requirements of T_{fo}, PM and GM and f_r. For example, if E_r is required to be 0.1%, then T_{fo}>60 dB; PM is generally selected between 30° and 60° to obtain good dynamic response; GM is generally greater than 3 dB to ensure sufficient robustness, the selection of f_r should refer to (10).

Step 2: According to the requirements in step 1, the expressions of $R_{\mathrm{ncl}}C_{f\_Tfo\_\mathrm{PM}}$ and $R_{\mathrm{ncl}}C_{f\_\mathrm{GM}}$ can be obtained by (19) and (21), respectively, so as to determine the feasible region of $R_{\mathrm{ncl}}C_f$. Fig. 11 shows the feasible region of $R_{\mathrm{ncl}}C_f$. The area below the red line meets the GM requirements, and the area above the blue line meets the requirements of T_{fo} and PM. The area enclosed by the two constraint lines is the feasible area of $R_{\mathrm{ncl}}C_f$. If the region is too small or does not exist, it is necessary to consider whether the requirements in step 1 are reasonable.

Step 3: Choose a suitable f_c within the feasible region. In order to improve the response speed and low-frequency gain, f_c can be high, but it should be lower than one-tenth of the switching frequency to ensure the switching harmonic suppression.

Step 4: R_{ncl} can be determined first according to the specific type of NCL, and then the appropriate C_f can be selected according to the margin requirement. Increasing $R_{\mathrm{ncl}}C_f$ will increase PM but not affecting T_{fo}. Therefore, if GM is sufficient, a larger $R_{\mathrm{ncl}}C_f$ should be met to improve dynamic response. L_{ff} can then be determined according to (8). K_p can be obtained according to (12).

Step 5: According to (16) and (18), the upper and lower limits of K_i are K_{i_Tfo} and K_{i_PM}, respectively. The larger the K_i, the smaller the steady-state error, but the worse the stability. After choosing the appropriate K_i, $G_i(s)$ can be tuned.

Step 6: Check whether the tuned loop frequency characteristic of $T_A(s)$ meets the design requirements in step 1.

The loop response before and after tuning can be obtained as shown in Fig. 12. It can be seen that the topology and control parameters obtained by the above design steps not only can suppress the resonance spike but also obtain the expected frequency characteristics.

TABLE I
SYSTEM PARAMETERS USED FOR SIMULATION

Elements	Parameters	Values
LCL-ES	Nominal power	30 kVA
	Switching frequency f_s	20 kHz
	DC-link voltage V_{dc}	800 V
	DC-link capacitor C_{dc}	1000 μF
	Grid side inductor L_{gf}	5 mH
	Converter side inductor L_{ff}	0.1 mH
	Filter capacitor C_f	10 μF
	a=2πfL_{gf}/R_{NCL}	0.314
Micro grid	Nominal phase voltage V_n	220 V
	Fundamental frequency f_o	50 Hz
	Line impedance R_g+jX_g	3.5+j2.5 Ω
Load	Critical load R_{cl}	14.44 Ω
	Non-critical Load R_{ncl}	5 Ω

V. SIMULATION AND DISCUSSION

Simulation verifications have been carried out base on Fig. 10, where the microgrid contains RESs and conventional loads with industry and domestic power profile. Parameters for simulation are given in Table I. For the simplicity and essentiality, only the pure reactive power mode of the *LCL*-ES is implemented here.

A. Case 1

The first case is to verify the PCC voltage regulation of *LCL*-ES, where *LCL*-ES is grid-synchronized when switch *S* is turned ON at 0.62 s, an overvoltage or undervoltage occurs at 1.5 s. As shown in Fig. 13(a), $V_{\mathrm{pcc\_rms}}$ rises up to 1.5 p.u., then *LCL*-ES increases the power of SL to counteract the overvoltage. After 6 or 7 fundamental cycles, $V_{\mathrm{pcc\_rms}}$ goes back around 220 V, which effectively verifies the ability to suppress the overvoltage. As shown in Fig. 13(b), $V_{\mathrm{pcc\_rms}}$ drops to less than 0.5 p.u. The power of SL begins to decrease to resist voltage drop. After about ten cycles, the PCC voltage returned to the normal range, which effectively verified the ability to suppress voltage sag.

B. Case 2

In order to compare the voltage regulation performance between series-ES and *LCL*-ES under the pure reactive power mode, a similar simulation by using series-ES was carried out. As shown in Fig. 14(a), $V_{\mathrm{pcc\_rms}}$ dropped to 0.6 p.u. at 1s, and

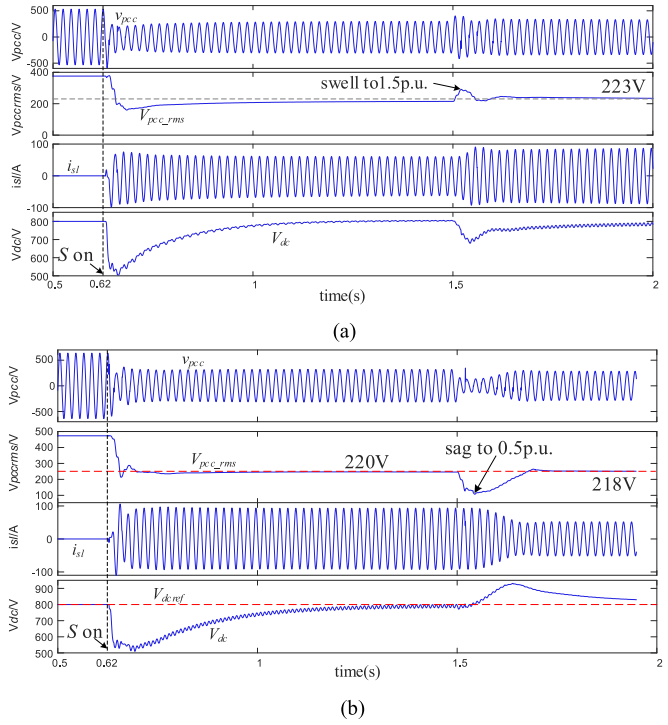

Fig. 13. Simulation results with *LCL*-ES. (a) Grid swell situation. (b) Grid sag situation.

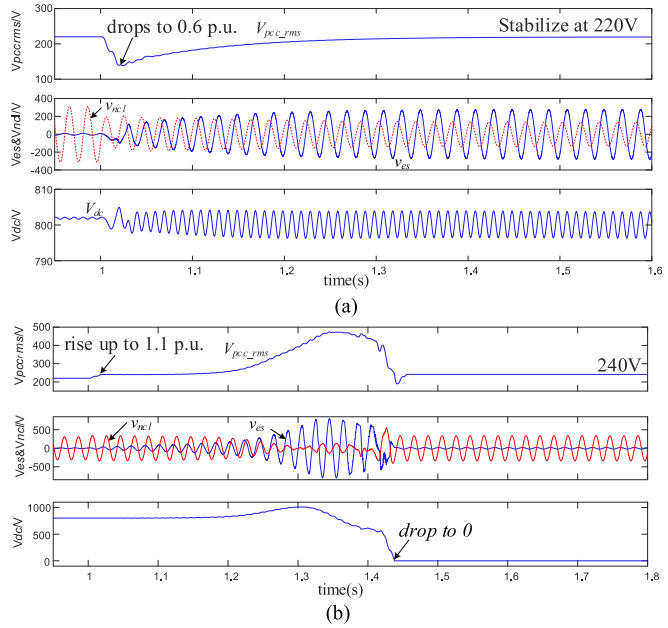

Fig. 14. Simulation results with series-ES. (a) Grid sag situation. (b) Grid swell situation.

stabilized at 220 V after about 0.3s under the action of series-ES, and V_{ncl} also decreased. At the same time, V_{dc} was stable around 800 V, which indicates that series-ES was working in pure reactive power mode. However, according to Fig. 14(b), even if PCC is slightly overvoltage to 1.1 p.u., the system eventually destabilized under the action of series-ES. Thus, series-ES has

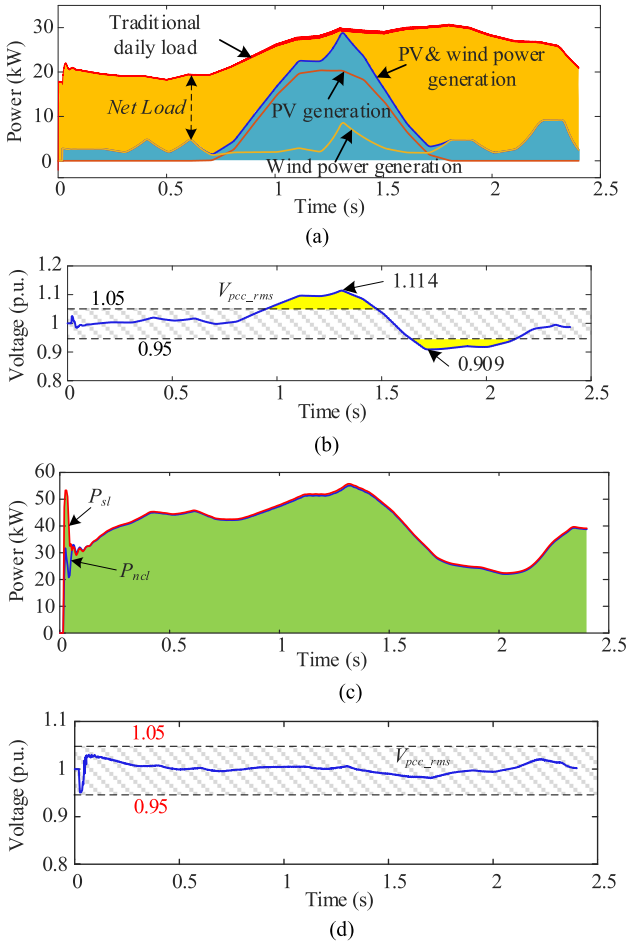

Fig. 15. Simulation results of case 3. (a) Daily characteristics of renewable energy and load power. (b) PCC voltage without *LCL*-ES (p.u.). (c) Powers of SL and NCL after *LCL*-ES is activated. (d) PCC voltage after *LCL*-ES is activated.

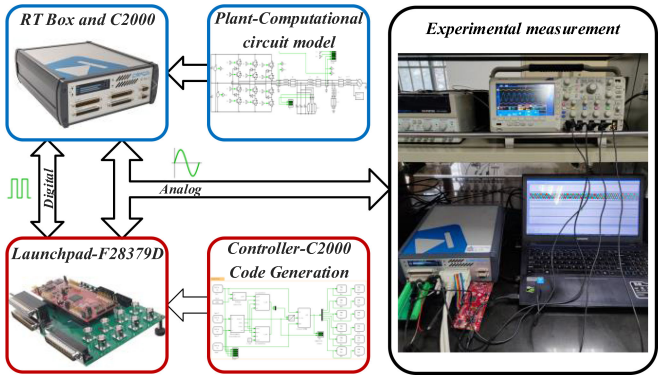

Fig. 16. Schematic for the established HIL platform and experimental setup.

a good compensation effect on the voltage sag of the grid, but it does not work under voltage swell as described in Section II.

C. Case 3

The third case is to simulate the 24-h power generation fluctuation of renewable energy in the microgrid and verify the voltage stabilization of *LCL*-ES. The 24-h traditional load, irradiance

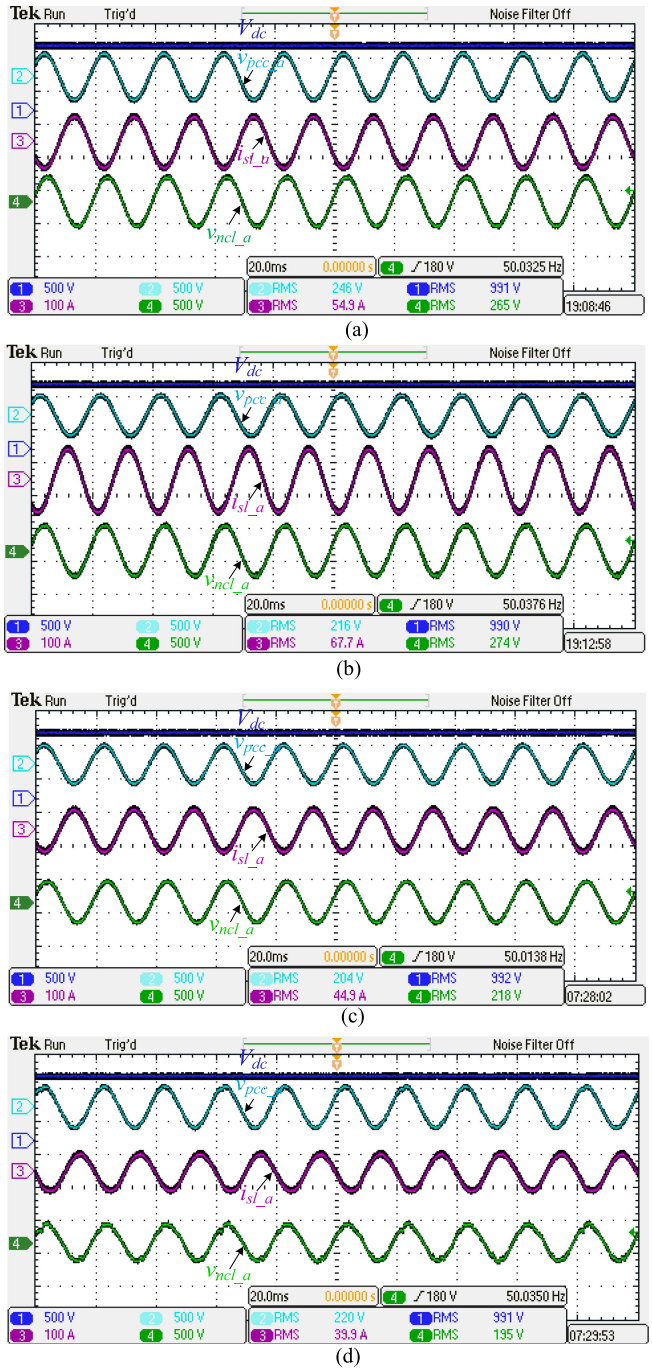

Fig. 17. Experimental results with resistive CL (phase a). (a) *LCL*-ES is not activated and $V_g = 664$ V. (b) *LCL*-ES is activated and $V_g = 664$ V. (c) *LCL*-ES is not activated and $V_g = 540$ V. (d) *LCL*-ES is activated and $= 540$ V.

and wind speed data are compressed to 2.4 s, the purpose is to emulate the fluctuation of DG and the typical traditional load within a day. The characteristics of the microgrid without *LCL*-ES were simulated firstly. As shown in Fig. 15(a) and (b), PV generation started from zero at 0.7s (7:00 A.M.) and reached a peak at about 1.2 s (12:00 A.M.), while wind power generation rose sharply at 1.3 s (1:00 P.M.), causing the total power of DG reach its peak value at this time. Although the load was rising, the net load of the microgrid (the difference between the

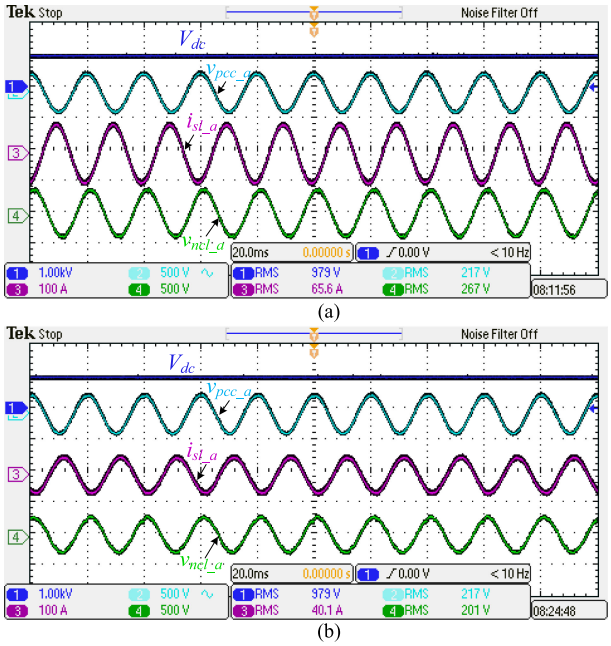

Fig. 18. Experimental results with inductive CL (phase a). (a) *LCL*-ES is activated and $V_g = 700$ V. (b) *LCL*-ES is activated and $V_g = 560$ V.

traditional load and DG) was decreasing, and $V_{\mathrm{pcc\_rms}}$ gradually rose and reached its peak at 1.3 s. After 1.4 s (2:00 P.M.), the DG power gradually dropped to a lower level and continued to fluctuate. Since the net load expanded first and then decreased, $V_{\mathrm{pcc\_rms}}$ fell below the limit and then rebounded. In Fig. 15(c) and (d), *LCL*-ES was activated and operated in pure reactive power mode. It is found that the fluctuation of the PCC voltage was significantly reduced.

VI. Experimental Results

To validate the voltage regulation function of the proposed *LCL*-ES practically, an experimental study has been conducted in RT-box, a hardware-in-the-loop (HIL) platform. The HIL tested integrates the microgrid model and control strategies discussed in previous sections for real-time microgrid testing. The main circuit of the microgrid and *LCL*-ES is established based on the parameters given in Table I. The control strategy and modulation methods are executed on digital signal processor. For the concision of the article, only the pure reactive power mode is presented. Fig. 16 shows the representation of the test setup, where the fluctuation of the grid voltage is emulated using adjustable three-phase voltage source.

In the first experiment, CL is 14.4 Ω and NCL is 5 Ω, which is reasonable for an electric–thermal load. When the grid voltage V_g rises to 664 V, it can be seen from Fig. 17(a) and (b) that the RMS of PCC voltage V_{PCC} swells to 246 V before *LCL*-ES is activated and goes back to 216 V after *LCL*-ES is activated. At the same time, the NCL voltage is also boosted from 265 to 274 V and an additional power of about 2910 W has been absorbed. In Fig. 17(c) and (d), when V_g falls to 540 V, V_{PCC} drops to 204 V when *LCL*-ES does not work. With the participation of *LCL*-ES,

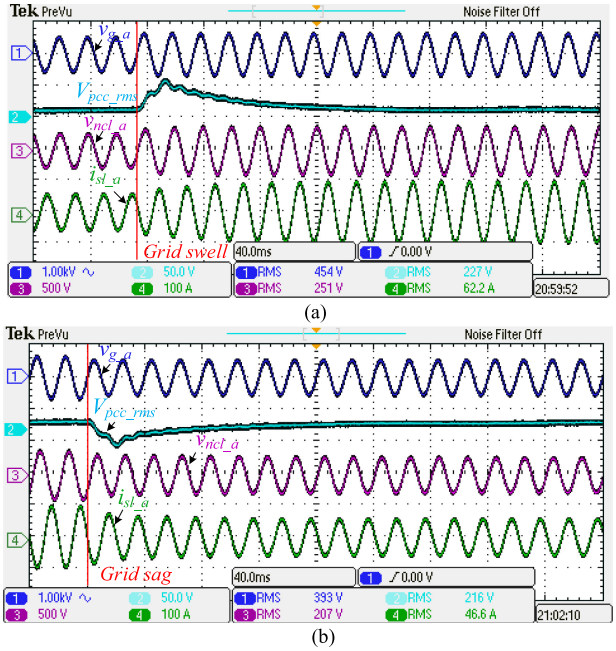

Fig. 19. Transition experimental results when ES is activated (phase a). (a) Grid swell. (b) Grid sag.

V_{PCC} rises back to 220 V and the NCL voltage is suppressed from 218 to 195 V.

In the second experiment, CL is replaced by an inductive load and its impedance is 50 Ω+1 mH. According to Fig. 18, it can be found that V_{PCC} remains stable regardless of whether the grid voltage rises or falls. At the same time, the NCL voltage has been effectively adjusted from 267 to 201 V.

Transition responses of *LCL*-ES are presented in Fig. 19. In order to observe the transient process, V_g in Fig. 19(a) swells to 1.15 times the normal value, while V_g in Fig. 19(b) sags to 0.87 times the normal value. It can be seen that although the grid voltage fluctuates rapidly, *LCL*-ES can stabilize the PCC voltage after about ten fundamental cycles. By observing the NCL voltage, it can be found that the power of NCL is indeed effectively adjusted to regulate the PCC voltage, and the demand response is very fast. When the grid swells, $P_{\rm sl}$ increases, and vice versa. The power characteristics of the *LCL*-ES is consistent with Fig. 6.

VII. Conclusion

A new construction method of ES has been proposed together with its preliminary design and control strategy, where the resistive NCL is used as the shunt damper for the *LCL* filter. The proposed *LCL*-ES has a more flexible and wider power range than the existing series-ES, and it can effectively realize the compensation of active and reactive power without energy storage unit to suppress grid sag and swell. Both the simulation and experimental results have verified the feasibility of *LCL*-ES. In general, *LCL*-ES can more fully utilize the potential of NCL as a demand response, which is critical for future power grid with a high proportion of distributed renewable sources.

References

[1] Y. Han, H. Li, P. Shen, E. A. A. Coelho, and J. M. Guerrero, "Review of active and reactive power sharing strategies in hierarchical controlled microgrids," *IEEE Trans. Power Electron.*, vol. 32, no. 3, pp. 2427–2451, Mar. 2017.

[2] T. Yang, K. T. Mok, S. S. Ho, S.-C. Tan, C.-K. Lee, and R. S. Y. Hui, "Use of integrated photovoltaic-electric spring system as a power balancer in power distribution networks," *IEEE Trans. Power Electron.*, vol. 34, no. 6, pp. 5312–5324, Jun. 2019.

[3] S. Y. Hui, C. K. Lee, and F. F. Wu, "Electric springs—A new smart grid technology," *IEEE Trans. Smart Grid*, vol. 3, no. 3, pp. 1552–1561, Sep. 2012.

[4] C. K. Lee, H. Liu, S. C. Tan, B. Chaudhuri, and S.-Y. R. Hui, "Electric spring and smart load: Technology, system-level impact and opportunities," *IEEE J. Emerg. Sel. Topics Power Electron.*, vol. 9, no. 6, pp. 6524–6544, Dec. 2021.

[5] S. C. Tan, C. K. Lee, and S. Y. Hui, "General steady-state analysis and control principle of electric springs with active and reactive power compensations," *IEEE Trans. Power Electron*, vol. 28, no. 8, pp. 3958–3969, Aug. 2013.

[6] S. Yan, S. C. Tan, C. K. Lee, B. Chaudhuri, and S. Y. R. Hui, "Use of smart loads for power quality improvement," *IEEE J. Emerg. Sel. Topics Power Electron.*, vol. 5, no. 1, pp. 504–512, Mar. 2017.

[7] K. T. Mok, S. S. Ho, S. C. Tan, and S. Y. Hui, "A comprehensive analysis and control strategy for nullifying negative-and zero-sequence currents in an unbalanced three-phase power system using electric springs," *IEEE Trans. Power Electron.*, vol. 32, no. 10, pp. 7635–7650, Oct. 2017.

[8] C. K. Lee and S. Y. Hui, "Input AC voltage control bi-directional power converters," U.S. Patent 13/907 350, May 31, 2013.

[9] S. Yan *et al.*, "Extending the operating range of electric spring using back-to-back converter: Hardware implementation and control," *IEEE Trans. Power Electron.*, vol. 32, no. 7, pp. 5171–5179, Jul. 2017.

[10] M. H. Wang, T. Yang, S. C. Tan, and S. Y. Hui, "Hybrid electric springs for grid-tied power control and storage reduction in AC microgrids," *IEEE Trans. Power Electron.*, vol. 34, no. 4, pp. 3214–3225, Apr. 2019.

[11] Q. Wang, M. Cheng, Z. Chen, and Z. Wang, "Steady-state analysis of electric springs with a novel δ control," *IEEE Trans. Power Electron.*, vol. 30, no. 12, pp. 7159–7169, Dec. 2015.

[12] K. T. Mok, S. C. Tan, and S. Y. Hui, "Decoupled power angle and voltage control of electric springs," *IEEE Trans. Power Electron.*, vol. 31, no. 2, pp. 1216–1229, Feb. 2016.

[13] Q. Wang, M. Cheng, Y. Jiang, W. Zuo, and G. Buja, "A simple active and reactive power control for applications of single-phase electric springs," *IEEE Trans. Ind. Electron.*, vol. 65, no. 8, pp. 6291–6300, Aug. 2018.

[14] G. Zhang *et al.*, "Forming a reliable hybrid microgrid using electric spring coupled with non-sensitive loads and ESS," *IEEE Trans. Smart Grid*, vol. 11, no. 4, pp. 2867–2879, Jul. 2020.

[15] Y. Yang, S. S. Ho, S. C. Tan, and S.-Y. R. Hui, "Small-signal model and stability of electric springs in power grids," *IEEE Trans. Smart Grid*, vol. 9, no. 2, pp. 857–865, Mar. 2018.

[16] N. R. Chaudhuri, C. K. Lee, B. Chaudhuri, and S. Y. R. Hui, "Dynamic modeling of electric springs," *IEEE Trans. Smart Grid*, vol. 5, no. 5, pp. 2450–2458, Sep. 2014.

[17] T. Yang, T. Liu, J. Chen, S. Yan, and S. Y. R. Hui, "Dynamic modular modeling of smart loads associated with electric springs and control," *IEEE Trans. Power Electron.*, vol. 33, no. 12, pp. 10071–10085, Dec. 2018.

[18] L. Liang, H. Yi, Y. Hou, and D. J. Hill, "An optimal placement model for electric springs in distribution networks," *IEEE Trans. Smart Grid*, vol. 12, no. 1, pp. 491–501, Jan. 2021.

[19] C. K. Lee, N. R. Chaudhuri, B. Chaudhuri, and S. Y. R. Hui, "Droop control of distributed electric springs for stabilizing future power grid," *IEEE Trans. Smart Grid*, vol. 4, no. 3, pp. 1558–1566, Sep. 2013.

[20] X. Chen, Y. Hou, and S. Y. Hui, "Distributed control of multiple electric springs for voltage control in microgrid," *IEEE Trans. Smart Grid*, vol. 8, no. 3, pp. 1350–1359, May 2017.

[21] J. Chen, S. Yan, T. Yang, S.-C. Tan, and S. Y. Hui, "Practical evaluation of droop and consensus control of distributed electric springs for both voltage and frequency regulation in microgrid," *IEEE Trans. Power Electron.*, vol. 34, no. 7, pp. 6947–6959, Jul. 2019.

[22] Y. Yang, Y. Qin, S. C. Tan, and S. Y. R. Hui, "Reducing distribution power loss of islanded AC microgrids using distributed electric springs with predictive control," *IEEE Trans. Ind. Electron.*, vol. 67, no. 10, pp. 9001–9011, Oct. 2020.

[23] M. Liserre, R. Teodorescu, and F. Blaabjerg, "Stability of photovoltaic and wind turbine grid-connected inverters for a large set of grid impedance values," *IEEE Trans. Power Electron.*, vol. 21, no. 1, pp. 263–272, Jan. 2006.
[24] Y. Han *et al.*, "Modeling and stability analysis of LCL-type grid-connected inverters: A comprehensive overview," *IEEE Access*, vol. 7, pp. 114975–115001, 2019.
[25] E. Fuchs and M. Masoum, *Power Quality in Power Systems and Electrical Machines*. San Diego, CA, USA: Academic, 2011.
[26] H. Fujita and H. Akagi, "Voltage-regulation performance of a shunt active filter intended for installation on a power distribution system," *IEEE Trans. Power Electron.*, vol. 22, no. 3, pp. 1046–1053, May 2007.
[27] A. Sadigh and K. Smedley, "Review of voltage compensation methods in dynamic voltage restorer (DVR)," in *Proc. IEEE Power Energy Soc. Gen. Meeting*, Jul. 2012, pp. 1–8.
[28] Y. Tang, P. C. Loh, P. Wang, F. H. Choo, F. Gao, and F. Blaabjerg, "Generalized design of high performance shunt active power filter with output LCL filter," *IEEE Trans. Ind. Electron.*, vol. 59, no. 3, pp. 1443–1452, Mar. 2012.
[29] M. Binam and E. Pashajavid, "An efficient procedure to design passive LCL-filters for active power filters," *Electr. Power Syst. Res.*, vol. 79, no. 4, pp. 606–614, Apr. 2009.
[30] D. Holmes, T. Lipo, B. McGrath, and W. Y. Kong, "Optimized design of stationary frame three-phase ac current regulators," *IEEE Trans. Power Electron.*, vol. 24, no. 11, pp. 2417–2426, Nov. 2009.
[31] A. Timbus, M. Liserre, R. Teodorescu, P. Rodriguez, and F. Blaabjerg, "Evaluation of current controllers for distributed power generation systems," *IEEE Trans. Power Electron.*, vol. 24, no. 3, pp. 654–664, Mar. 2009.

Dongyuan Qiu (Member, IEEE) received the B.Sc. and M.Sc. degrees from the South China University of Technology, Guangzhou, China, in 1994 and 1997, respectively, and the Ph.D. degree from the City University of Hong Kong, Hong Kong, in 2002.

She is currently a Professor with the School of Electric Power, South China University of Technology, Guangzhou, China. She has authored or coauthored 4 books, and more than 100 papers and holds more than 100 patents. Her main research interests include modeling and control of power electronic converters, wireless power transfer, and fault diagnosis of power electronic systems.

Dr. Qiu is currently an Associate Editor for the IEEE TRANSACTIONS ON POWER ELECTRONICS.

Changhai Yuan was born in China in 1995. He received the B.S. degree from Nanchang University, Nanchang, China, in 2018, and the M.S. degree from the School of Electric Power Engineering, South China University of Technology, Guangzhou, China, in 2021, both in electrical engineering.

In 2017, he was with Global Data Solutions Ltd. His current research interests include power supply and distribution systems and renewable energy applications in data centers.

Bo Zhang (Senior Member, IEEE) was born in Shanghai, China, in 1962. He received the B.S. degree in electrical engineering from Zhejiang University, Hangzhou, China, in 1982, the M.Sc. degree in power electronics from Southwest Jiaotong University, Chengdu, China, in 1988, and the Ph.D. degree in power electronics from the Nanjing University of Aeronautics and Astronautics, Nanjing, China, in 1994.

He is currently a Professor with the School of Electric Power, South China University of Technology, Guangzhou, China. He has authored or coauthored 10 books and more than 500 technical papers and holds more than 150 patents. His current research interests include nonlinear analysis, modeling and control of power electronic converters, and wireless power transfer applications.

Mingbin Ke was born in China in 1997. He received the B.S. degree in electrical engineering and automation in 2019 from the South China University of Technology, Guangzhou, China, where he is currently working toward the M.S. degree in electrical engineering with the School of Electric Power.

His research interests include analysis and application of electric spring, and power electronic converters.

Yanfeng Chen (Member, IEEE) received the M.S. degree in power electronics technology from Wuhan University, Wuhan, China, in 1995, and the Ph.D. degree in circuits and systems from the South China University of Technology, Guangzhou, China, in 2000.

From August 2000 to December 2002, she was a Postdoctoral Researcher with the Department of Electronics Engineering, Sun Yat-Sen University, Guangzhou, China. From November 2005 to December 2006, she was a Research Associate with the Department of Electronic and Information Engineering, Hong Kong Polytechnic University, Hong Kong. She is currently a Professor with the School of Electric Power, South China University of Technology. She has authored or coauthored 3 books and more than 50 papers and holds more than 50 patents. Her main research interests include modeling and analysis of nonlinear systems and power electronics.

Fan Xie (Member, IEEE) received the B.S. and M.S. degrees in physics and physical electronics from the School of Physics and Electron Engineering, Guangzhou University, Guangzhou, China, in 2008 and 2011, respectively, and the Ph.D. degree in power electronics from the South China University of Technology, Guangzhou, China, in 2014.

In 2014, he was with the School of Electric Power, South China University of Technology, Guangzhou, China, where he has been an Associate Professor since 2018. His research interests include nonlinear dynamics of power electronic circuits and control of power supplies and ac drives.